# Seismic discrimination of controlled explosions and earthquakes near Mount St. Helens using P/S ratios

Ruijia Wang[1*], Brandon Schmandt[1], & Eric Kiser[2]

1. Department of Earth and Planetary Science, University of New Mexico, Albuquerque, NM, 87131, USA.

2. Department of Geosciences, University of Arizona, Tucson, AZ, 85721, USA.

*Corresponding author: ruijia.wang@ualberta.ca.

**Key Points:**

1. Influences on local P/S ratios are analyzed with 23 shallowly buried explosions and 406 $M_L \geq 1$ earthquakes near Mount St. Helens.
2. Optimized array-median P/S ratios discriminate explosions with 100% true positives and 4.93% false positives.
3. P/S ratio variations at individual stations are interpreted as site effects that correlate with shallow crustal velocity structure.

# Abstract

Explosions and earthquakes are effectively discriminated by P/S amplitude ratios for moderate magnitude events (M≥4) observed at regional to teleseismic distances (≥200 km). It is less clear if P/S ratios are effective explosion discriminants for lower magnitudes observed at shorter distances. We report new tests of P/S discrimination using a dense seismic array in a continental volcanic arc setting near Mount St. Helens, with 23 single-fired borehole explosions ($M_L$ 0.9-2.3) and 406 earthquakes ($M_L$ 1-3.3). The array provides up to 95 three-component broadband seismographs and most source-receiver distances are <120 km. Additional insight is provided by ~3,000 vertical component geophone recordings of each explosion. Potential controls on local distance P/S ratios are investigated, including: frequency range, distance, magnitude, source depth, number of seismographs, and site effects. A frequency band of 10-18 Hz performs better than lower or narrower bands because explosion-induced S-wave amplitudes diminish relative to P for higher frequencies. Source depth and magnitude exhibited negligible influences. Site responses for earthquakes and explosions are correlated with each other and with shallow crustal Vp and Vs from travel-time tomography. Overall, the results indicate high potential for local distance P/S discrimination in a continental volcanic arc setting, with 100% true positives and 4.93% false positives using a frequency band of 10-18 Hz for array-median P/S ratios.



# Plain Language Summary

Methods to remotely classify seismic sources as either shear-slip earthquakes or shallow subsurface explosions are important geophysical tools. They are used for investigations of anthropogenic processes such as underground nuclear explosion tests and mining activity as well as to obtain pure catalogs of tectonic and volcanic earthquakes. The ratio of compressional (P) wave amplitude to shear (S) wave amplitude is effective for classifying large earthquakes and explosions observed hundreds to thousands of kilometers away. Application of such methods at local distances is a topic of growing interest because smaller magnitude sources are only observed at close distances. We tested influences on P/S amplitude ratios and their effectiveness for source discrimination using a data set of tectonic and volcanic earthquakes and controlled shallow borehole explosions near Mount St. Helens. Most observations were within 120 km. We found that use of high frequencies and array-median statistics is largely effective for source

discrimination in this setting, successfully classifying 100% of explosions while falsely attributing about 5% of earthquakes to explosions. Variability of P/S ratios across the seismic array has a highly similar pattern for explosions and earthquakes and that pattern appears to be controlled by the seismic velocity structure of the shallow crust.

# 1. Introduction

Quantifying the distinctive properties of explosive seismic sources is an important capability for identification and characterization of underground nuclear explosion tests and a key component of verifying compliance with nuclear test-ban treaties (Bowers and Selby, 2009). Seismic identification and characterization of explosions are also important in other contexts, such as investigations of chemical explosions that may be the subjects of judicial investigations (e.g., Holzer et al., 1996; Koper et al., 2002, 2003) and volcanic explosions studied in the interest of natural hazard mitigation (e.g., Neuberg et al., 1994; Rowe et al., 1998; Johnson and Lees, 2000). Early research on seismic discrimination of nuclear explosions and earthquakes focused on events that are observable at regional to teleseismic distances (≥200 km), which generally requires M≥4 (Richards and Zavales, 1990). One useful seismic approach to discriminating nuclear explosions and earthquakes at such distances is the measurement of P/S amplitude ratios. Abundant empirical evidence confirms that large explosions (M≥4) produce greater P/S amplitude ratios compared to tectonic earthquakes, although the observed ratios are regionally heterogeneous (Taylor et al., 1989; Kim et al., 1993; Walter et al., 1995; Hartse et al., 1997; Xie and Patton, 1999; Jenkins and Sereno, 2001).

Potential expansion of seismic discrimination techniques to local distances and lower magnitudes (or explosive yields) has become a subject of increasing interest (Zeiler and Velasco, 2009; O'Rourke et al., 2016; Kolaj, 2018; Pyle and Walter, 2019; Holt et al., 2019; Kinter et al., 2020). At local distances and lower magnitudes, methods are usually developed to discriminate chemical explosions from earthquakes and, in some cases, to differentiate single-fired explosions from delayed-fired explosions that are common in mining activity (Zeiler and Velasco, 2009; O'Rourke et al., 2016). Single-fired chemical explosions in boreholes provide a useful proxy for underground nuclear tests (Stump et al., 1999) and well-documented examples are available for study on account of geophysical experiments targeting seismic source physics (e.g., Pyle and Walter, 2019) or imaging of geological structures (e.g., O'Rourke et al., 2016). There is mixed evidence regarding the effectiveness of P/S discrimination for ≤M3 events at distances of ≤200 km. Some empirical investigations report that failure to discriminate between earthquakes and explosions may be restricted to the shortest distances (e.g., ≤50 km in O'Rourke et al., 2016). Others report sporadic failures across the local distance range, potentially on account of lithologic variability of the crust causing complex source and path effects that are more subdued

at regional to teleseismic distances (e.g., Pyle and Walter, 2019). Further research is needed to address questions such as: Does the complexity of crustal wave propagation make P/S ratios less diagnostic of explosive sources below a common distance threshold? Can diminished explosion discrimination performance be overcome by larger seismic arrays or enhanced local calibration using earthquakes to constrain site and/or path effects? What are the underlying differences in explosion sources that control discrimination capability at local distances?

We use a data set with dense local distance recordings of earthquakes and single-fired borehole explosions near Mount St. Helens to gain further insight into the seismic source and structural properties that control the effectiveness of the P/S ratio explosion discriminant for low yields (Fig. 1). Important aspects of the data set are its diverse source-receiver paths with most distances <120 km and its combination of single-fired borehole explosions and earthquakes, including shallow volcanic seismicity at Mount St. Helens (e.g., Ulberg et al., 2020; Glasgow et al., 2018). The source-receiver distribution was optimized for 3D structural imaging, so the source locations are not limited to one isolated test site or linear transect. The inclusion of volcanic earthquakes near Mount St. Helens offers an interesting comparison because volcanoes often produce more frequent shallow earthquakes and more variable source mechanisms compared to other geologic settings.

## 2. Data

This study uses seismic recordings of earthquakes and single-fired chemical explosions in shallow boreholes (Table S1). The explosions were detonated for the controlled source component of the iMUSH project to image the magmatic system underlying Mount St. Helens (Kiser et al., 2016, 2018; Hansen et al., 2016). Eight of the 23 boreholes were loaded with 907 kg of explosive and the other 15 were loaded with 454 kg (Fig. 1b). The explosives were buried in shallow boreholes with maximum depths of ~22-28 m and explosives occupying the bottom ~5 m of the boreholes. Earthquake source information from 2014 - 2016 was provided by the Pacific Northwest Seismic Network, which contributes to the USGS Comprehensive Catalog (ComCat; USGS, 2020). Earthquakes within 75 km of Mount St. Helens with $M_L \geq 1$ were considered for the study. Lower magnitude earthquakes were not clearly recorded across most of the study area so most seismograms would be removed by the requirement of signal-to-noise (SNR) >2.

Additionally, using $M_L \geq 1$ provides a close match to the magnitude range of the explosions ($M_L$ 0.9-2.3).

The primary seismic waveform data for this study are from the broadband part of the iMUSH project (Han et al., 2018; Crosbie et al., 2019; Mann et al., 2019; Ulberg et al., 2020), which temporarily increased the density of local seismic monitoring. The iMUSH broadband network (XD 2014-2016) was combined with permanent regional three-component broadband stations to create a composite network of up to 95 stations within 75 km of Mount St. Helens (Fig. 1a). Sampling rates vary among the networks. Based on the minimum sample rate of 40 Hz we limited our analysis to frequencies ≤18 Hz. Network information for all the broadband data is provided in Table S1. Examples of explosion and earthquake record sections from the broadband array are shown in Figure 2. The example events have equal local magnitudes ($M_L$=1.9) and they are plotted after application of bandpass filtering from 2-6 Hz. The explosion source exhibits a stronger P-wave than the earthquake, while the earthquake exhibits a more prominent S-wave than the explosion (Fig. 2).

A secondary source of seismic waveform data is vertical-component geophones deployed during the iMUSH controlled source imaging experiment (Kiser et al., 2016, 2018; Hansen et al., 2016). Our analysis of source discrimination using P/S energy focuses on three-component recordings so we only present record sections from the vertical geophones to illustrate local phase propagation (Fig. 3). In Figure 3, the geophone seismograms for all 23 explosions (70,944 source-receiver pairs) were sorted into 1 km distance bins and the median envelope in each distance bin is plotted with trace-normalized amplitude. The high density of recordings illustrates the existence of the S-wave starting at small distances and extending across the array. Comparison of the 2-6 Hz envelopes in Figure 3a and 6-18 Hz envelopes in Figure 3b shows diminished S-wave amplitudes relative to P for higher frequencies. Due to the short duration of the geophone deployment and movement of most geophones during the experiment, there are few opportunities for comparison with earthquakes that were recorded across most of the array. Consequently, we focus on the broadband data from 2014 - 2016 for evaluation of P/S ratio as an explosion versus earthquake discriminant.

# 3. Methods

## 3.1 P/S amplitude ratios

P/S ratios were measured with an approach similar to that used by O'Rourke et al. (2016). Below we focus on the subtle differences with respect to use of three-component data and phase windowing for amplitude measurements. O'Rourke et al. (2016) omitted the transverse components for P measurements because a 1D isotropic medium should not produce P-wave energy on the transverse component. In contrast to O'Rourke et al. (2016), we use all three components for measurements of amplitude in P, S, and pre-event noise windows for both earthquakes and explosions. P-wave energy is commonly observed on transverse components in our dataset (Fig. 2), presumably due to out-of-plane scattering.

Phase windowing at local distances presents a challenge due to the decreasing separation of P and S with decreasing distance. To maximize use of the data we scaled the window length by the S-P time, so that the time window length increases with distance until reaching a fixed duration. The time window starts at -5% of the S-P time before the phase arrival time (P, S or Noise) and ends at 50% of the S-P time after the arrival time for shorter source-receiver distances. At larger distances (i.e., beyond 40 km) a fixed value of 3 sec after the arrival time (Fig. 4) is used for the end of the measurement window. Stations that are too close to an event (i.e., produce a S-P time window less than 1 sec) are discarded because they prevent reliable separation of P and S amplitudes and their arrival times are more variable. Pre-event noise time windows were sampled starting at 10 sec before the origin time of each explosion or earthquake source. Our goal is to ensure the maximum phase energy is captured within the windows while minimizing the contamination from noise or interfering phases. Although the optimization of phase-windowing is somewhat arbitrary, consistent P/S ratio results were achieved in additional tests with the maximum window length increased to 4, 5, and 6 sec. We focus on the 3 sec window results for the remainder of the text.

The phase windows shown in Figure 4 were calculated using a local 1D P and S velocity model derived from the controlled source survey (Fig. 1b and Fig. S1; Kiser et al., 2016). Events with P-wave root-mean-square amplitude SNR>2 were retained for P/S ratio measurements (Fig. S2). Stability in the results for different phase window lengths from 3-6 sec indicates that the

deviations from the predicted 1D arrival times have little effect. This is not surprising because phase picks for the explosion sources from Ulberg et al., (2020) have small travel time residuals compared to the 3 sec window length (Fig. 4). Residual times for 1309 manually picked P phases from explosions recorded by the broadband array have a standard deviation of 0.3 sec (average 0.01 sec), much smaller than our window width. Manual picks are unavailable for many P and S phases at individual stations because only the clearest arrivals are picked. Thus, we prefer the generic phase windowing approach using the 1D velocity model and 3 sec phase windows for consistency and to avoid biasing amplitude measurements by under-representing weak S-waves that are important to source discrimination.

After phase windowing the three-component P/S ratio ($R$) at a given station (n) was calculated as:

$$R_n = \frac{\sqrt{P_i^2 - N_i^2}}{\sqrt{S_i^2 - N_i^2}}, \quad \text{Eq(1)}$$

where the subscript i denotes summation of the three seismogram components. For source discrimination tests, the array median and scaled median absolute deviation (SMAD) of all the individual P/S ratios are used. P/S ratios were measured with waveforms bandpass filtered in several frequency bands. We tested narrow frequency bands of 2-4 Hz, 4-6 Hz, 6-8 Hz, 8-10 Hz, 10-12 Hz,12-14 Hz, and 14-16 Hz, following O'Rourke et al., (2016). We also tested two broader frequency bands of 6-12 Hz and 10-18 Hz. In each case a two-pole Butterworth filter was applied to the response-corrected waveforms after demeaning and detrending.

## 3.2 Bootstrap resampling for different array sizes

The temporary broadband array (XD), in combination with the permanent networks (UW, CC), provides better seismic sampling than is available for many areas of interest for explosion monitoring (Fig. 1a). Although up to 95 stations are available during the 2-year period, not all stations/components are available the entire time and meet the SNR>2 threshold. Within our preferred frequency range (10-18Hz), the number of stations that are finally used for P/S ratio calculation for explosions ranges from 36 to 78, with an average of 66. The average number of stations for $M_L \geq 2$ and $M_L$1-2 earthquakes are 72 and 47, respectively. To fully evaluate the potential of our preferred method and parameter set, we used bootstrap resampling test to

simulate results for six subset array sizes: 2, 4, 8, 16, 32, and 64. For each subset, the cumulative array was randomly resampled 1,000 times (without replacement) from the 74 common stations that recorded all earthquakes and explosions without any prerequisite (i.e., SNR). Within each sampled set, the array-median P/S ratio for earthquakes and explosions are calculated after applying the SNR control. In the other words, the bootstrapping approach attempts to simulate scenarios with smaller arrays and an unconditioned distribution of SNR recordings.

### 3.3 Site corrections for P/S ratios

We estimated station-based site corrections using P/S ratios of earthquakes. This was chosen to mimic the circumstance in which P/S corrections could be estimated using only earthquake data and then applied to subsequent events of unknown physical origin. The correction is calculated as a normalization of event-averaged P/S ratio at each of the N stations:

$$C_{1,2,3\ldots N} = R_{eq@station(1,2,3,..n)} / \mathrm{mean}(R_{eq@station(1,2,3,..n)}), \qquad \text{Eq(2)}$$

Where, $R_{eq@station(1,2,3,..n)}$ is a vector that contains N values, each corresponding to an event-averaged P/S ratio (i.e., calculated from up to 406 earthquakes) at a given station after the SNR control. For each event (explosion or earthquake) recorded at a subset of m stations, its P/S ratio is then corrected by dividing $C_{1,2,3\ldots m}$. The outcome of site correction is discussed in section 4.5 and $R_{eq}$ for the entire array is presented in Figure 9b.

## 4. Results

### 4.1 Optimal frequency content

Array median P/S ratios for explosions are greater than for earthquakes in all frequency bands (Fig. 5). However, the one SMAD intervals of P/S ratios overlap for lower frequency bands and most narrow frequency bands. Distributions of P/S ratios are typically not Gaussian (i.e., long-tailed), so the SMAD is preferred instead of the standard deviation. In general, higher bands provide larger separation in the median P/S ratios between earthquakes and explosions, while broader bands help to decrease the variance and stabilize discrimination of individual events (Fig. 5). With respect to source discrimination, 10-18 Hz is the preferred frequency band for this local distance data set. The 14-16 Hz band also performs well but for individual events it is more

variable and may reduce the number of SNR>2 phase windows for analysis. The 10-18 Hz array-median P/S ratios and SMAD values for earthquakes and explosions are 1.72(±0.34) and 0.46(±0.19), respectively. P/S ratios for both earthquakes and explosions increase with frequency, however the increase with frequency is greater for the explosions (Fig. 5). This result from analysis of the three-component broadband array data is consistent with the observation from the vertical-component geophones showing that S-wave amplitude diminishes relative to P for higher frequencies (Fig. 3).

## 4.2 Distance, magnitude, and depth effects

We focus on results from distances <120 km because most of the available source-receiver pairs are within that distance range (Fig. 4b). Median P/S ratios for earthquakes and explosions sorted into six 20 km wide distance bins show little change at shorter distances and then increasing P/S ratio with distance beyond ~60 km (Fig. 6a). The SMAD values are also larger at greater distances due to the decreased number of samples within each distance bin. Given that distance distributions of earthquakes and explosions are very similar in this study (Fig. 4b), we do not apply distance corrections to the P/S ratios.

P/S ratios for earthquakes and explosions do not vary strongly with local magnitude (Fig. 5b). The median P/S ratios in most 0.2 $M_L$ bins overlap within one SMAD. There appears to be an increase in P/S ratio for the largest explosion magnitude bin, but it is heavily influenced by one explosion source with a particularly high P/S ratio resulting in a relatively large SMAD for the highest magnitude bin among explosions (Fig. 5b). Earthquake P/S ratios remain low across the local magnitude range. There is a slight decrease in the median earthquake P/S ratios for the largest magnitudes ($M_L$>2.5), which is within the range of one SMAD. Given the weak distance and magnitude dependences found in the P/S ratios, we did not apply the magnitude and distance amplitude correction (MDAC) approach that is commonly used in regional distance studies (Anderson et al., 2009).

Estimated earthquake source depths also do not exhibit a clear correlation with P/S ratios (Fig. 7). As the area near Mount St. Helens is characterized by variable surface topography (i.e., ranging from 0 - 4 km, Fig. 1), we also take the topography into account and calculate the relative distance to the surface (instead of absolute depth to sea level). Binning the earthquake sources into four depth ranges (0-5, 5-10, 10-15, and 15-20 km) results in median P/S ratios that

all overlap with one SMAD. Depth uncertainties are highly variable depending on local array coverage, but reported uncertainties from the Pacific Northwest Seismic Network for $M_L \geq 1$ earthquakes near Mount St. Helens are typically <1 km. In that context, results from binning within 5-km depth intervals should not be strongly biased by inaccurate depth estimates. There is a slight decrease in median P/S ratio from 0.3 at 0-5 km to 0.26 at 15-20 km, which is within the SMAD (i.e., 0.07-0.14) for any of the source depth bins.

## 4.3 Number of stations in the seismic array

Bootstrap resampling of the three-component seismographs simulates the potential average source discrimination performance with smaller seismic arrays (see section 3.2). The cumulative distribution functions (CDFs) from resampling show that greater variations are observed for explosion P/S ratios compared to earthquake P/S ratios (Fig. 8). Increasingly large seismic arrays help reduce the overlap of earthquake and explosion P/S ratio distributions near a value of ~1 (Fig. 8). Separation of earthquake and explosion P/S ratios is subject to diminishing improvement for arrays with over 16 stations. The improvement with increasing array size appears modest in this context because the curves shown in Figure 8 are generated as averages from 1,000 bootstrap resampling subsets (for 2, 4, 8, 16, 32 and 64 station cases). The variance of P/S ratios is much larger for smaller arrays and its effect on discrimination performance is discussed further in section 5.1.

## 4.4 Site response effects and shallow crust structure

Variations in station-averaged P/S ratios from earthquakes and borehole explosions exhibit similar spatial patterns, despite the generally higher P/S ratios for explosions (Fig. 9). A scatter plot of the earthquake station-averages versus the explosion station-averages shows an approximately linear trend, with a correlation coefficient of 0.625. If the earthquakes are subset by magnitude, the $M_L$1-2 and $M_L \geq 2$ subsets yield correlations of 0.625 and 0.641 (these two earthquake subsets are correlated at 0.91), respectively. These correlations indicate that observations of small (~$M_L$1-3) earthquakes may provide a useful basis for determining empirical P/S amplitude site corrections that are applicable to explosions. However, the improvement for the purpose of source discrimination appears to be subtle in this case (Fig. 10).

Application of site corrections increased the difference between the median explosion and earthquake P/S ratios from 1.29 to 1.41, but the SMAD values also increased slightly for explosions (0.38 to 0.43) and earthquakes (0.21 to 0.23). Furthermore, we found the site correction terms are positively correlated with shallow crustal velocities. We adopted a velocity model from a recent local travel time tomography study around Mount St. Helens (Ulberg et al., 2020) and compared our site corrections with the Vp, Vs and Vp/Vs values beneath all the station (site) locations. At 1km depth, the cross-correlation coefficients for the site correction terms are 0.397 for Vp and 0.479 for Vs. Site corrections exhibit a much weaker correlation of -0.086 with Vp/Vs (Fig. 9 d-f). The correlation coefficients remain comparable for all layers around sea level (±2km) and they decrease at deeper depths, suggesting that the site correction is influenced by uppermost crustal structure.

# 5. Discussion

## 5.1 Effectiveness for explosion discrimination

Receiver operating characteristic (ROC) curves show the diagnostic performance of binary classifiers, in this case for explosions versus earthquakes, using a variety of discrimination thresholds (Fig. 11). For each P/S ratio used as a discrimination threshold the point along the ROC curve is determined by the rate of true positives and false positives. The optimal discrimination threshold is chosen by maximizing the area under the curve (AUC), thus an ideal classifier would plot in the upper left corner corresponding to 100% true positive and 0% false positives. Application to P/S ratios with the preferred frequency band of 10-18 Hz and the full data set of earthquakes and explosions shows 100% true positives and 4.93% (20 out of 406) false positives for a P/S ratio threshold of 1.2 (Fig. 11a). Half of the events that create false positives (i.e., P/S>1.2) are only recorded with <6 stations, reflecting the disadvantage of insufficient station coverage for low-magnitude sources (Fig. S3). For comparison, a lower and narrower frequency band of 6-8 Hz results in 86.95% true positives and 5.67% false positives for a P/S ratio threshold of 0.9.

Discrimination performance generally improves with increasing event magnitude and array size (Fig. 11c, d). Using all explosions and only $M_L \geq 2$ earthquakes, a threshold P/S ratio of 1.2 results in 100% true positives and 0% false positives. The $M_L$ 0.9-2.3 explosions produced an

average of 66 stations with SNR>2, while the $M_L$ 1-2 earthquakes only produced an average of 47 stations with SNR>2. So, the diminished discrimination performance for $M_L$1-2 earthquakes is likely influenced by SNR at individual stations and the total number of stations available for analysis. ROC curves for seismic arrays composed of N=4, 16, and 64 seismographs illustrate the effects of array size (Fig. 11c). For N=64, the bootstrap resampling results show that a maximum AUC of 1 is consistently achieved for discrimination of explosions and $M_L \geq 2$ earthquakes. For N=16, the average of the AUC maxima is 0.98. For N=4, the average of the AUC maxima reduces to 0.94 (Fig. 11d). However, the ROC curves for N=4 are much more variable, including a few samples with near-random performance (Fig. 11c) and some extreme cases reaching the AUC maximum (Fig. 11d). Generally, larger array size is expected to better mitigate source/path variations. A separate bootstrap resampling test with an earthquake epicenter nearly co-located with an explosion shows that <16 stations are sufficient for robust discrimination (Fig. S4), suggesting that minimum number of stations could be much lower if the earthquake and suspected explosion are closely located with depth difference (i.e., as an ideally case). In this example the horizontal locations are separated by 2.4 km and the depths are separated by 11.1 km.

Comparison of the new results from near Mount St. Helens with other local distance P/S ratio discrimination tests may be influenced by different local propagation effects related to geological settings as well as measurement approaches. A similar scale study using data covering the Bighorn mountain range and adjacent sedimentary basins in Wyoming found effective P/S discrimination at ~50-200 km distance but failure at <50 km distance (O'Rourke et al., 2016). Below we consider two minor methodological differences between this study and O'Rourke et al. (2016) that might contribute to the difference in performance. We acknowledge that different local propagation effects may also be the cause of the difference, but a thorough re-analysis of their data would be required to isolate that influence.

The first methodological difference is that we include the transverse component for P-wave measurements (see section 3.1). Explosion recordings in this study commonly show SNR>2 (our threshold for analysis) even for P-waves recorded on the transverse component (Fig. 2). If scattering of P energy onto the transverse component is important at distances <50 km, then the inclusion of transverse component data may be beneficial for explosion discrimination. A comparison of array-median P/S ratios with and without the transverse component shows that

separation of the explosion and earthquake ratios improves with inclusion of the transverse component (Fig. 12). The increased separation is primarily due to increases in the explosion P/S ratios, while changes in the earthquake P/S ratios are smaller. This is consistent with the possibility that out-of-plane P-wave scattering is stronger for explosions than earthquakes. In this case, the benefit of including transverse component P-wave energy spans our entire local distance range (Fig. 12), but given that P/S ratios tend to increase with distance for both approaches the incremental improvement is more important at smaller distances (≤60 km).

The second difference is that we did not apply the MDAC method for regional seismic discriminants (Anderson et al., 2009) to correct for distance and magnitude effects. We chose not to use MDAC because the distance and especially magnitude trends in our raw P/S ratios are modest compared to the SMAD values for explosion and earthquakes, respectively (Fig. 6). Additionally, O'Rourke et al. (2016) note that stations at their shortest distances (~20-40 km) exhibit abnormally high MDAC corrections for explosions. We speculate that the amplitude correction techniques developed for regional distances may need to be revised for shorter local distances. Similar to the weak distance and magnitude trends found in this study, Zeiler and Velasco (2009) reported negligible distance dependence of explosion discriminants (including P/S ratios) within the local distance range. We suggest that the necessity and design of the amplitude correction techniques for explosions observed at short distances (≤50 km) should be further investigated.

In a recent local to regional distance study, Pyle and Walter (2019) investigated P/S ratio discrimination with six chemical explosions from the Source Physics Experiment (Snelson et al., 2013) and nearby tectonic earthquakes. Similar to O'Rourke et al. (2016) and this study, Pyle and Walter (2019) found that P/S discrimination performance improved with increasing frequency (≥6 Hz) and that array averaging of ~10 or more stations was needed to achieve clear separation of explosion and earthquake P/S ratios. Four of the six explosions used in their study had larger explosive yields than all the explosions in this study and the receiver spacing within ~100 km was sparser, so relative to O'Rourke et al., (2016) there is less opportunity for comparison of results at similar scales. The fact that we observe optimal performance for somewhat higher frequencies in this study (e.g., 10-18 Hz) likely reflects our focus on shorter source-receiver distances of <120 km compared to distances up to ~450 km in Pyle and Walter, (2019).

## 5.2 Source effects

The geophone record sections show that S-waves emerge within the first few kilometers from the source, acknowledging that there is not sufficient sampling available to resolve S-wave emergence in detail at scales of hundreds of meters (or less) from the source (Fig. 3). Assuming the S-wave is effectively generated at the source for this data set, increasing P/S ratio with distance is expected if S-wave attenuation is greater than P-wave attenuation in the crust (e.g., Pyle et al., 2017). In contrast, a difference in source spectra may be needed to explain why explosion P/S ratios increase with frequency more than earthquake P/S ratios (Fig. 5).

Prior studies of M≳3 chemical explosions and nuclear explosions indicate that explosion-induced crustal S-waves (Lg) exhibit lower corner frequencies than explosion-induced P-waves (local Pg & regional Pn phases; Xie, 2002; Fisk, 2006, 2007). In these studies, the S-wave corner frequency is typically about half of the P-wave corner frequency. Our results with lower yield chemical explosions are similar based on the increased separation of local distance explosion and earthquake P/S ratios at higher frequencies. The 10-18 Hz band may perform relatively well for P/S ratio discrimination because it partially overlaps the interval between the lower S-wave corner frequency and the higher P-wave corner frequency (e.g., Fisk, 2007). Using the Mueller-Murphy model corner frequency scaling from Fisk, (2007) the explosions in this study are expected to produce local P-wave corner frequencies of ~35-45 Hz and S-wave corner frequencies of ~17-23 Hz (Fig. S5). The 40 Hz sampling rate for most stations limited our analysis to frequencies below ~18 Hz, so only the highest frequencies in this study are near the expected S-wave corner. Extension of P/S ratio measurements to higher frequencies by collecting higher sample-rate data may be beneficial, especially for very short distances (≤50 km) and low magnitudes ($M_L \leq 2$).

The physical controls on explosion-induced S-wave spectra remain debated. If a difference in source spectra explains the observed frequency dependence of P/S ratios, the physical cause may be rooted in the different P and S elastic length scales of sensitivity to near-source rock damage (Taylor, 2009). However, a variety of complicated and locally specific effects such as spall and free-surface topographic scattering are thought to influence explosion-induced S-wave spectra so there may not be one dominant explanation (e.g., Xie and Lay, 1994; Patton and Taylor, 1995). An alternative to explaining the frequency dependence of P/S ratios

with different source spectra is that explosions may preferentially excite shallower shear modes that attenuate more rapidly with distance (e.g., Baker et al., 2004, 2012).

One explosion source in this study that produced a relatively low P/S ratio resulted in clear surface evidence of shear slip at the source. The 'X4' explosion (Fig. 1b; also see Table S1) detonated in a borehole with maximum depth of ~22 m depth resulted in a small normal fault scarp with a length of ~15 m and vertical offset of up to ~20 cm. Consequently, it is unsurprising that this explosion exhibited a relatively low P/S ratio of 1.27 (Fig. 10), which is near the optimal binary classification cutoff of 1.2 for 10-18 Hz the data set including all $M_L \geq 1$earthquakes (Fig. 11b). It is unknown if 'blind' shear failures that did not rupture the surface are common for other low P/S ratio explosions.

## 5.3 Combining local distance seismic discriminants

Ratios of different seismic magnitude metrics such as mb & Ms have long been used as an initial or 'screening' step for source discrimination of $M \gtrsim 3$ events (Stevens and Day, 1985; Selby et al., 2012; Ford and Walter, 2014). At local scales there is growing evidence that the difference between the local (Richter) magnitude and the coda duration magnitude ($M_L$-$M_C$) can help discriminate explosions, primarily because the magnitude difference is sensitive to source depth (Holt et al., 2019; Voyles et al., 2020). Very shallow sources such as borehole explosions preferentially produce longer coda leading to negative $M_L$-$M_C$. P/S amplitude ratios ignore the extended coda and we find negligible depth dependence for P/S amplitude ratios in this study (Fig. 7). Thus, the capabilities of the two discriminants appear to be rooted in complementary aspects of the local seismic wavefield. A simple workflow to leverage the two approaches would be using $M_L$-$M_C$ to screen for unusual events given that routine catalog generation can commonly provide both parameters. Then events identified by screening could be further investigated with P/S ratios. More thorough approaches to jointly classifying events based on $M_L$-$M_C$ and P/S ratios should also be considered. P/S ratio measurements could also be automated to enhance screening capabilities once travel time relationships and site corrections are developed for an array. Additional use of more time-consuming moment tensor analysis of low magnitude local distance events might be reserved for events flagged by $M_L$-$M_C$ and P/S screening (e.g., Alvizuri and Tape, 2016).

# 6. Conclusions

P/S ratio discrimination of earthquakes and shallow single-fired borehole explosions at distances less than 120 km was tested with a dense broadband seismic array near Mount St. Helens. Taking advantage of the excellent coverage of both stations and sources, we evaluated the effects of frequency bands, source-receiver distances, source magnitudes and focal depths. Optimal separation of P/S ratios for the two sources types was found using a 10-18 Hz frequency band, which achieved explosion discrimination with 100% true positives and 4.93% false positives using the entire array. Randomly resampling to simulate smaller arrays shows performance of ≥98% true positives and ≤6.3% false positives for ≥16 stations. Performance becomes highly variable using ≤4 stations. Successful separation using the dense array and optimized frequency band left limited room to improve the performance, consequently our site corrections derived from 406 local earthquakes had a negligible effect on discrimination statistics. Despite the limited improvements in this case, we found that the site corrections correlate with Vp and Vs of the uppermost crust from a recent tomography study. Future studies using P/S ratios may benefit from local site corrections derived from small earthquake recordings or local tomography models.

# Acknowledgements

Seismic waveform data used in the study are publicly accessible via the IRIS DMC (http://ds.iris.edu/ds/nodes/dmc/data/) using the network information provided in Table S1. The IRIS DMC is supported by the National Science Foundation under Cooperative Support Agreement EAR-1851048. Eli Baker and Keith Koper provided helpful feedback during the research. Carl Ulberg shared phase picks and a local tomography model. This research was supported by the Air Force Research Lab under contract No. FA9453-19-C-0055.

# References

Alvizuri, C., & Tape, C. (2016). Full moment tensors for small events (M w< 3) at Uturuncu volcano, Bolivia. *Geophysical Journal International*, *206*(3), 1761-1783.

457 Anderson, D. N., Walter, W. R., Fagan, D. K., Mercier, T. M., & Taylor, S. R. (2009). Regional
458 multistation discriminants: Magnitude, distance, and amplitude corrections, and sources
459 of error. *Bulletin of the Seismological Society of America*, *99*(2A), 794-808.
460 Baker, G. E., Stevens, J. L., & Xu, H. (2012). Explosion shear-wave generation in low-velocity
461 source media. *Bulletin of the Seismological Society of America*, *102*(4), 1320-1334.
462 Baker, G. E., Stevens, J., & Xu, H. (2004). Lg group velocity: A depth discriminant revisited.
463 *Bulletin of the Seismological Society of America*, *94*(2), 722-739.
464 Crosbie, K. J., Abers, G. A., Mann, M. E., Janiszewski, H. A., Creager, K. C., Ulberg, C. W., &
465 Moran, S. C. (2019). Shear velocity structure from ambient noise and teleseismic surface
466 wave tomography in the Cascades around Mount St. Helens. *Journal of Geophysical*
467 *Research: Solid Earth*, *124*(8), 8358-8375.
468 Fisk, M. D. (2006). Source spectral modeling of regional P/S discriminants at nuclear test sites in
469 China and the former Soviet Union. *Bulletin of the Seismological Society of America*,
470 *96*(6), 2348-2367.
471 Fisk, M. D. (2007). Corner frequency scaling of regional seismic phases for underground nuclear
472 explosions at the Nevada Test Site. *Bulletin of the Seismological Society of America*, *97*(3),
473 977-988.
474 Glasgow, M. E., Schmandt, B., & Hansen, S. M. (2018). Upper crustal low-frequency seismicity
475 at Mount St. Helens detected with a dense geophone array. *Journal of Volcanology and*
476 *Geothermal Research*, *358*, 329-341.
477 Han, J., Vidale, J. E., Houston, H., Schmidt, D. A., & Creager, K. C. (2018). Deep long-period
478 earthquakes beneath Mount St. Helens: Their relationship to tidal stress, episodic tremor
479 and slip, and regular earthquakes. *Geophysical Research Letters*, *45*(5), 2241-2247.
480 Hansen, S. M., Schmandt, B., Levander, A., Kiser, E., Vidale, J. E., Abers, G. A., & Creager, K.
481 C. (2016). Seismic evidence for a cold serpentinized mantle wedge beneath Mount St
482 Helens. *Nature communications*, *7*(1), 1-6.
483 Holt, M. M., Koper, K. D., Yeck, W., D'Amico, S., Li, Z., Hale, J. M., & Burlacu, R. (2019). On
484 the Portability of ML–M c as a Depth Discriminant for Small Seismic Events Recorded at
485 Local Distances. Bulletin of the Seismological Society of America, 109(5), 1661-1673.

Holzer, T. L., Fletcher, J. B., Fuis, G. S., Ryberg, T., Brocher, T. M., & Dietel, C. M. (1996). Seismogram offers insight into Oklahoma City bombing. *Eos, Transactions American Geophysical Union*, *77*(41), 393-399.

Jenkins, R. D., & Sereno Jr, T. J. (2001). Calibration of regional S/P amplitude-ratio discriminants. *Pure and Applied Geophysics*, *158*(7), 1279-1300.

Johnson, J. B., & Lees, J. M. (2000). Plugs and chugs—seismic and acoustic observations of degassing explosions at Karymsky, Russia and Sangay, Ecuador. *Journal of Volcanology and Geothermal Research*, *101*(1-2), 67-82.

Kim, W. Y., Simpson, D. W., & Richards, P. G. (1993). Discrimination of earthquakes and explosions in the eastern United States using regional high-frequency data. *Geophysical research letters*, *20*(14), 1507-1510.

Kintner, J. A., Michael Cleveland, K., Ammon, C. J., & Nyblade, A. (2020). Testing a Local-Distance R g/S g Discriminant Using Observations from the Bighorn Region, Wyoming. *Bulletin of the Seismological Society of America*, *110*(2), 727-741.

Kiser, E., Palomeras, I., Levander, A., Zelt, C., Harder, S., Schmandt, B., Hansen, S.M., Creager, K.C., & Ulberg, C. (2016). Magma reservoirs from the upper crust to the Moho inferred from high-resolution Vp and Vs models beneath Mount St. Helens, Washington State, USA. *Geology*, *44*(6), 411-414.

Kiser, E., Levander, A., Zelt, C., Schmandt, B., & Hansen, S. (2018). Focusing of melt near the top of the Mount St. Helens (USA) magma reservoir and its relationship to major volcanic eruptions. *Geology*, *46*(9), 775-778.

Kolaj, M. (2018). Discriminating between low-magnitude shallow earthquakes and road construction blasts near Big Salmon River, New Brunswick, Canada. *Seismological Research Letters*, *89*(5), 1966-1976.

Koper, K. D., Wallace, T. C., Reinke, R. E., & Leverette, J. A. (2002). Empirical scaling laws for truck bomb explosions based on seismic and acoustic data. *Bulletin of the Seismological Society of America*, *92*(2), 527-542.

Koper, K. D., Wallace, T. C., & Aster, R. C. (2003). Seismic recordings of the Carlsbad, New Mexico, pipeline explosion of 19 August 2000. *Bulletin of the Seismological Society of America*, *93*(4), 1427-1432.

Mann, M. E., Abers, G. A., Crosbie, K., Creager, K., Ulberg, C., Moran, S., & Rondenay, S. (2019). Imaging subduction beneath Mount St. Helens: Implications for slab dehydration and magma transport. *Geophysical Research Letters*, *46*(6), 3163-3171.

Neuberg, J., Luckett, R., Ripepe, M., & Braun, T. (1994). Highlights from a seismic broadband array on Stromboli volcano. *Geophysical Research Letters*, *21*(9), 749-752.

O'Rourke, C. T., Baker, G. E., & Sheehan, A. F. (2016). Using P/S amplitude ratios for seismic discrimination at local distances. *Bulletin of the Seismological Society of America*, *106*(5), 2320-2331.

Patton, H. J., & Taylor, S. R. (1995). Analysis of Lg spectral ratios from NTS explosions: Implications for the source mechanisms of spall and the generation of Lg waves. *Bulletin of the Seismological Society of America*, *85*(1), 220-236.

Pyle, M. L., Walter, W. R., & Pasyanos, M. E. (2017). High-Resolution 2D Lg and Pg Attenuation Models in the Basin and Range Region with Implications for Frequency-Dependent QHigh-Resolution 2D Lg and Pg Attenuation Models in the Basin and Range Region with Implications. *Bulletin of the Seismological Society of America*, *107*(6), 2846-2858.

Pyle, M. L., & Walter, W. R. (2019). Investigating the Effectiveness of P/S Amplitude Ratios for Local Distance Event Discrimination. Bulletin of the Seismological Society of America, 109(3), 1071-1081.

Rowe, C. A., Aster, R. C., Kyle, P. R., Schlue, J. W., & Dibble, R. R. (1998). Broadband recording of Strombolian explosions and associated very-long-period seismic signals on Mount Erebus Volcano, Ross Island, Antarctica. *Geophysical research letters*, *25*(13), 2297-2300.

Selby, N. D., Marshall, P. D., & Bowers, D. (2012). mb: M s event screening revisited. *Bulletin of the Seismological Society of America*, *102*(1), 88-97.

Snelson, C. M., Abbott, R. E., Broome, S. T., Mellors, R. J., Patton, H. J., Sussman, A. J., Townsend, M. J., & Walter, W. R. (2013). Chemical explosion experiments to improve nuclear test monitoring. *Eos, Transactions American Geophysical Union*, *94*(27), 237-239.

Stevens, J. L., & Day, S. M. (1985). The physical basis of mb: Ms and variable frequency magnitude methods for earthquake/explosion discrimination. *Journal of Geophysical Research: Solid Earth*, *90*(B4), 3009-3020.

Stump, B. W., Pearson, D. C., & Reinke, R. E. (1999). Source comparisons between nuclear and chemical explosions detonated at Rainier Mesa, Nevada Test Site. *Bulletin of the Seismological Society of America*, *89*(2), 409-422.

Taylor, S. R., Denny, M. D., Vergino, E. S., & Glaser, R. E. (1989). Regional discrimination between NTS explosions and western US earthquakes. *Bulletin of the Seismological Society of America*, *79*(4), 1142-1176.

Taylor, S. R. (2009). Can the Fisk conjecture be explained by rock damage around explosions?. *Bulletin of the Seismological Society of America*, *99*(4), 2552-2555.

Ulberg, C. W., Creager, K. C., Moran, S. C., Abers, G. A., Thelen, W. A., Levander, A., Kiser, E., Schmandt, B., Hansen, S.M., & Crosson, R. S. (2020). Local source Vp and Vs tomography in the Mount St. Helens region with the iMUSH broadband array. *Geochemistry, Geophysics, Geosystems*. DOI: 10.1029/2019GC008888.

USGS (2020). ANSS comprehensive earthquake catalog (ComCat).

Voyles, J. R., Holt, M. M., Hale, J. M., Koper, K. D., Burlacu, R., & A. Chambers, D. J. (2020). A New Catalog of Explosion Source Parameters in the Utah Region with Application to ML–MC-Based Depth Discrimination at Local Distances. *Seismological Research Letters*, *91*(1), 222-236.

Walter, W. R., Mayeda, K. M., & Patton, H. J. (1995). Phase and spectral ratio discrimination between NTS earthquakes and explosions. Part I: Empirical observations. *Bulletin of the Seismological Society of America*, *85*(4), 1050-1067.

Walter, W R, and Taylor, S R. (2001). A Revised Magnitude and Distance Amplitude Correction (MDAC2) Procedure for Regional Seismic Discriminants: Theory and Testing at NTS. United States: N. p., Web. doi:10.2172/15013384.

Xie, X. B., & Lay, T. (1994). The excitation of Lg waves by explosions: A finite-difference investigation. *Bulletin of the Seismological Society of America*, *84*(2), 324-342.

Xie, J. (2002). Source scaling of Pn and Lg spectra and their ratios from explosions in central Asia: Implications for the identification of small seismic events at regional distances. Journal of Geophysical Research: Solid Earth, 107(B7), ESE-1.

Zeiler, C., & Velasco, A. A. (2009). Developing local to near-regional explosion and earthquake discriminants. *Bulletin of the Seismological Society of America*, *99*(1), 24-35.

577 Zhang, J., Lay, T., Zaslow, J., & Walter, W. R. (2002). Source effects on regional seismic
578 discriminant measurements. Bulletin of the Seismological Society of America, 92(8),
579 2926-2945
580

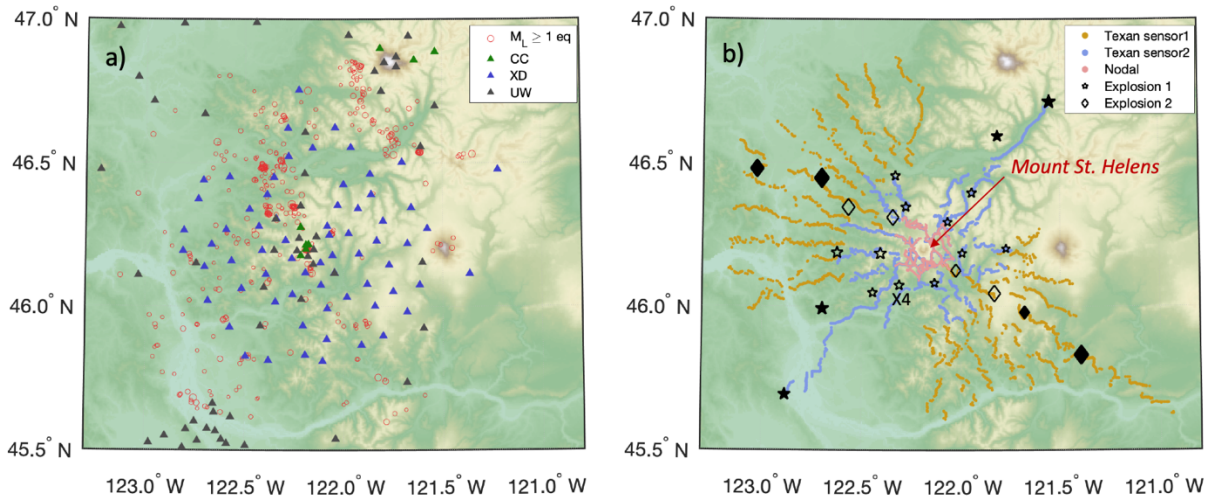


581

582 Figure 1. Study area maps with sources and receivers. A) Broadband stations used in the study
583 are plotted along with the locations of $M_L \geq 1$ earthquakes that occurred between June 20, 2014 to
584 August 31, 2018 (i.e., time span for XD array) within 75 km of Mount St. Helens. B) Vertical
585 geophone locations are plotted along with single-fired explosion locations. Explosion locations
586 loaded with 907 kg of explosive are denoted by filled symbols and locations loaded with 454 kg
587 are denoted by hollow symbols. The symbol sizes for explosions are scaled by their $M_L$.
588 Explosions labeled with stars were detonated during controlled source phase 1 (recorded by
589 Texan 1 array; ~2370 nodes) and diamonds were detonated during phase 2 (recorded by Texan 2
590 array; ~2220 nodes). 'X4' denotes one explosion that is discussed in the text. Geophone
591 locations in pink (~900 nodes) recorded both sets of explosions.

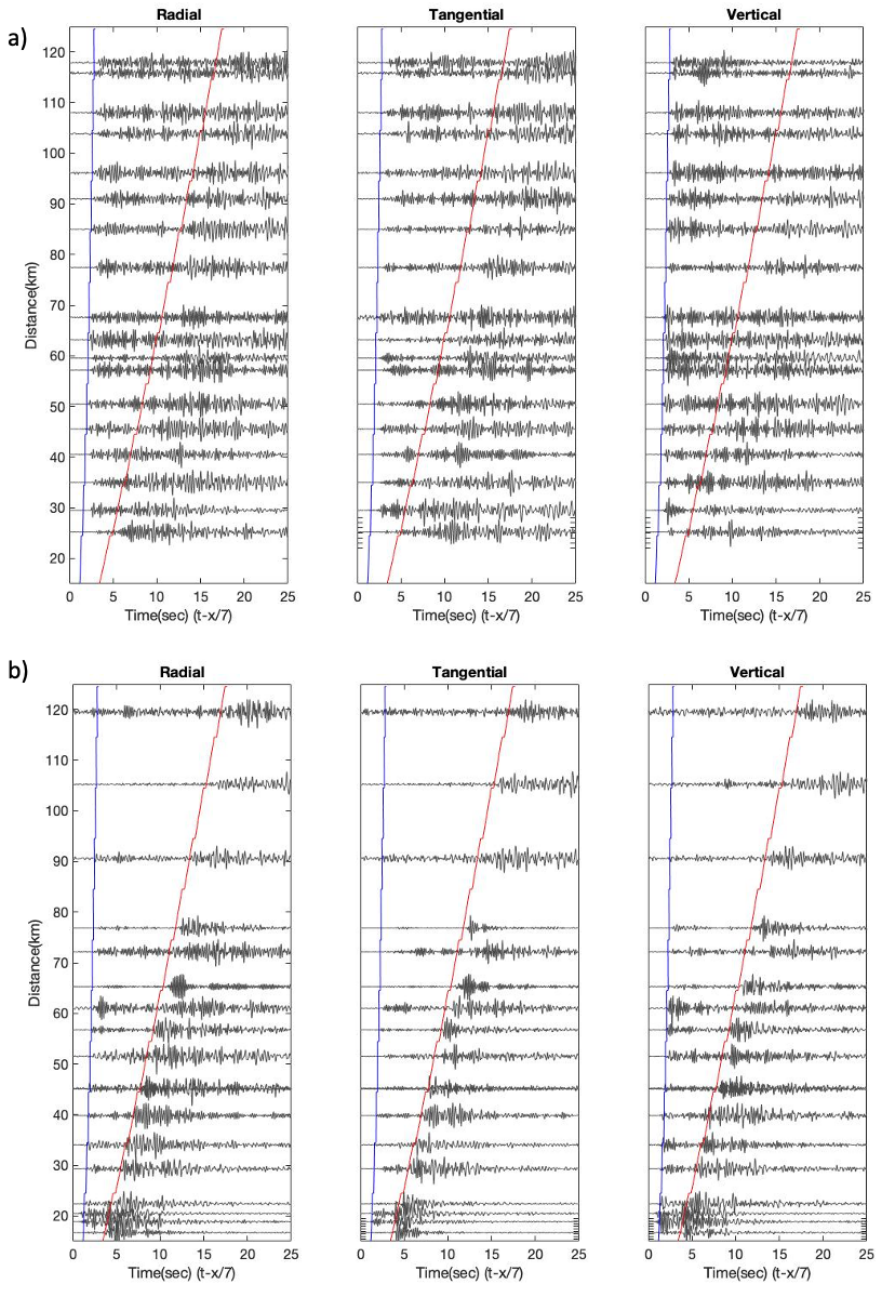


Figure 2. A) A record section is plotted for an explosion event with 616kg equivalent TNT load (Y8, located at the NW of array, $M_L$=1.9; see Table S1 for details). The event showed relatively strong S energy among explosions. Only 18 seismograms are shown for clarity. B) Record section for an equal-magnitude earthquake (2015 Feb 9, 05:45:35) with waveforms from 19 stations. Waveforms are filtered between 2-6 Hz at plotted with a reduced velocity of 7 km/s in both figures. The blue and red lines mark the predicted P and S wave arrivals, respectively, using a locally optimized 1D velocity model (Kiser et al., 2016; also see Fig. S1).

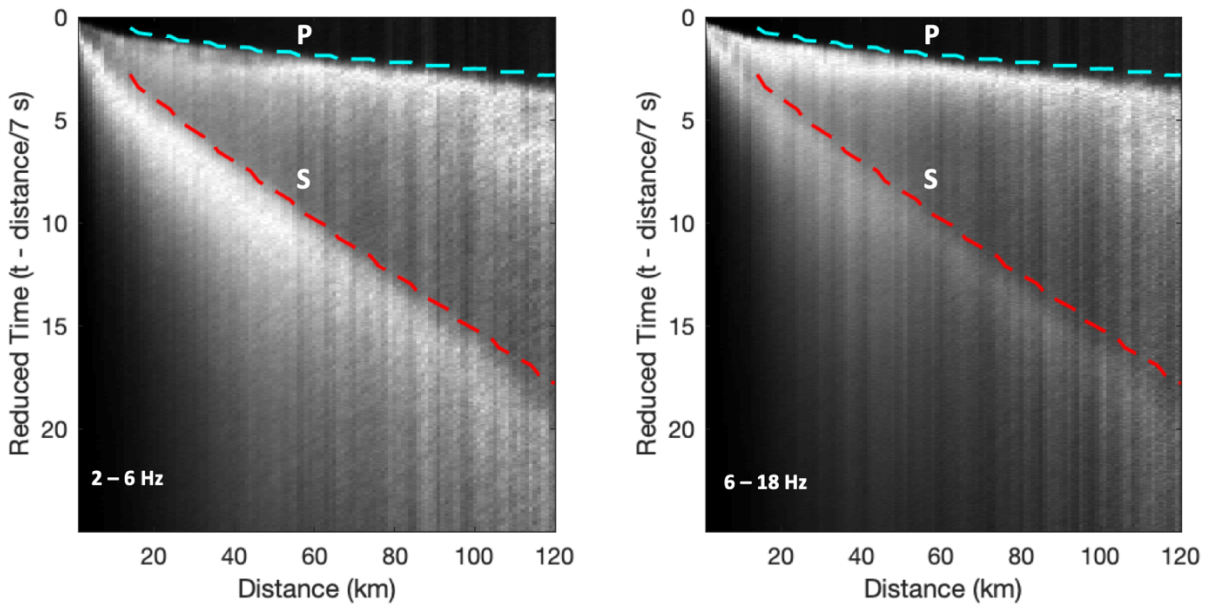


Figure 3. Stacked geophone recordings of explosions. A) Median envelopes of geophone seismograms from all 23 explosions in 1 km distance bins (70,944 source-receiver pairs). Seismograms were bandpass filtered from 2-6 Hz before envelope calculation and median-stacking. Median envelopes at each distance are normalized by their maximum. The cyan dashed line marks the beginning of the P window and the red dashed line marks the beginning of the S window. B) Same as A, except that seismograms were bandpass filtered from 6-18 Hz. The higher frequency band exhibits diminished S-wave amplitudes relative to P.

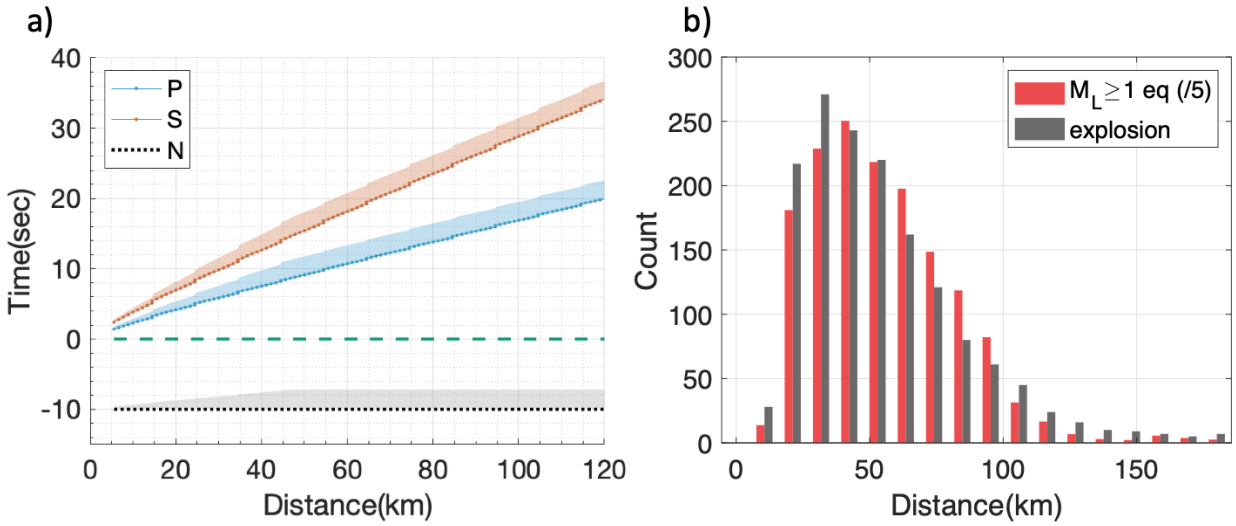


Figure 4. Phase windowing and source-receiver distances. A) Phase windowing based on travel times from a local 1D P and S velocity model (Kiser et al., 2016). B) Histogram of source-receiver distances using 10 km bins up to 180 km. Note that the number of earthquake source-receiver pairs in each distance bin is divided by 5 to better enable comparison of the two distributions.

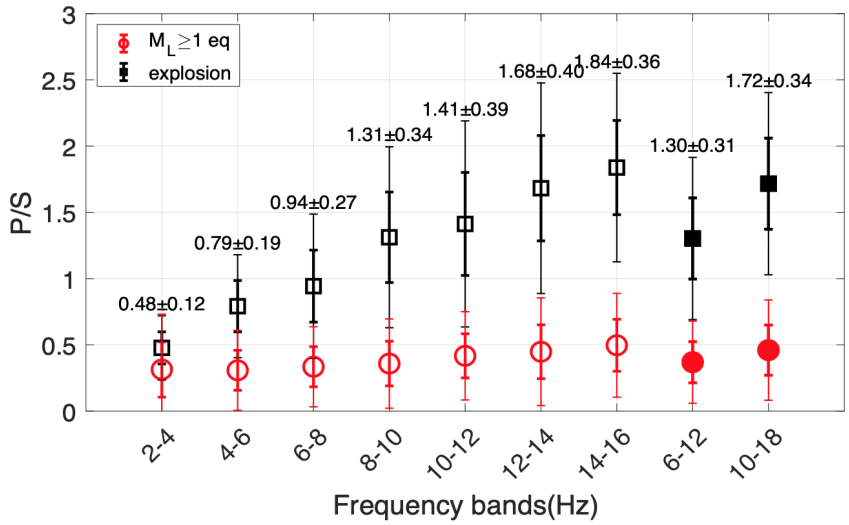


Figure 5. Median P/S ratio for explosions and earthquakes at nine different frequency bins: seven 2-Hz narrow bins same as O'Rourke et al., 2016 and two wide bins (filled symbols). Bold error bars are SMAD and thin bars are 2-scaled median absolute deviation (i.e., 2*SMAD). The median±SMAD for explosions are labeled on top.

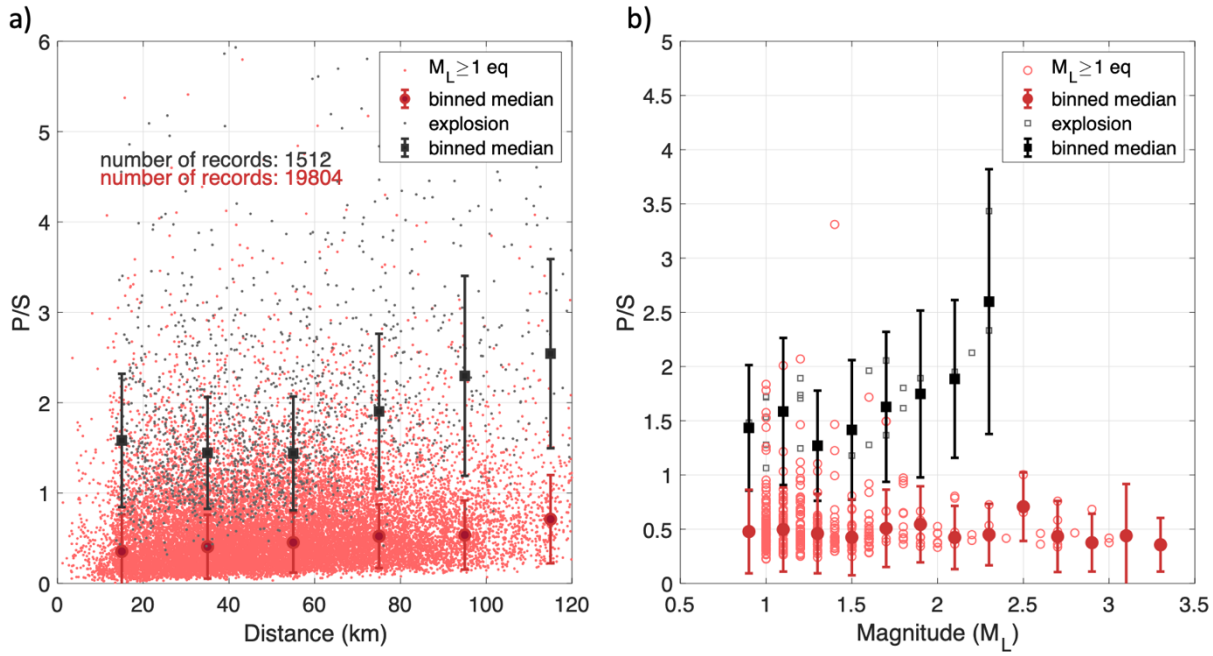


Figure 6. Distance and magnitude effects. A) P/S versus distance averaged over 20 km with step size of 20 km for all source-station pairs of earthquakes and explosions. B) P/S ratio versus magnitudes with bin size of 0.2. Error bars indicate the SMAD calculated from station-based ratios of all events within each magnitude bin.

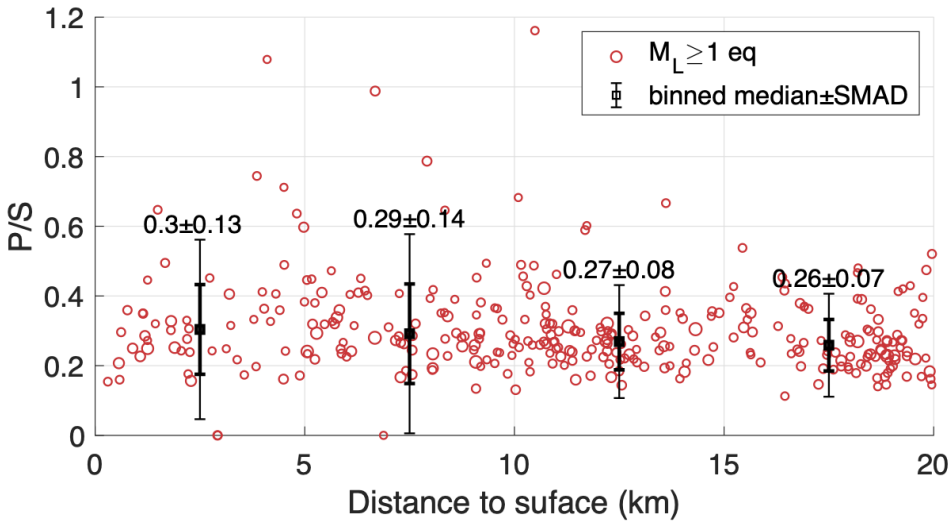


Figure. 7. Earthquake P/S ratios versus source depth below surface. Red circles show array-averaged P/S ratios for individual earthquakes, with circle size scaled by $M_L$ (1-3.3). The four bold (thin) bars show median SMAD (2*SMAD) within depth bins: 0-5 km, 5-10 km, 10-15 km, and 15-20 km.

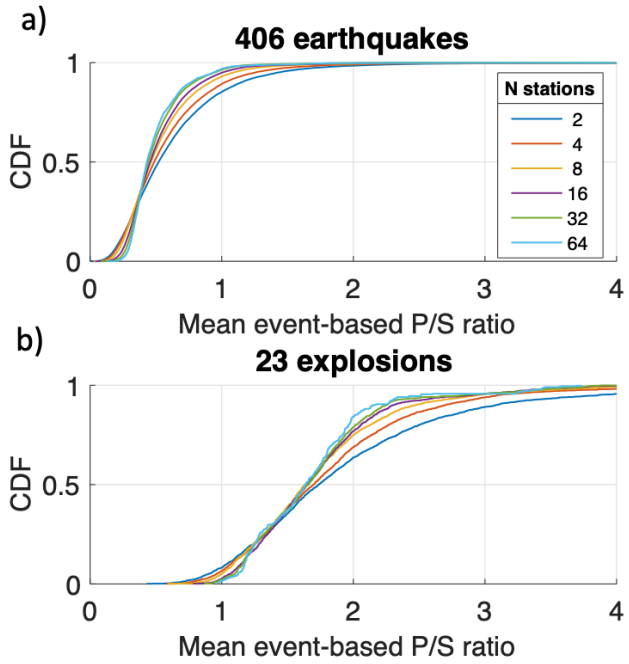


Figure 8. Effects of array size on P/S ratios. A) Cumulative distribution functions (CDF) for P/S ratios of earthquakes as a function of array size for 2, 4, 8, 16, 32, and 64 stations. Each event ratio is calculated from the median of P/S ratio measured at N stations while the final CDF curves are generated from the mean of all events. B) Same as (A) except for explosions rather than earthquakes.

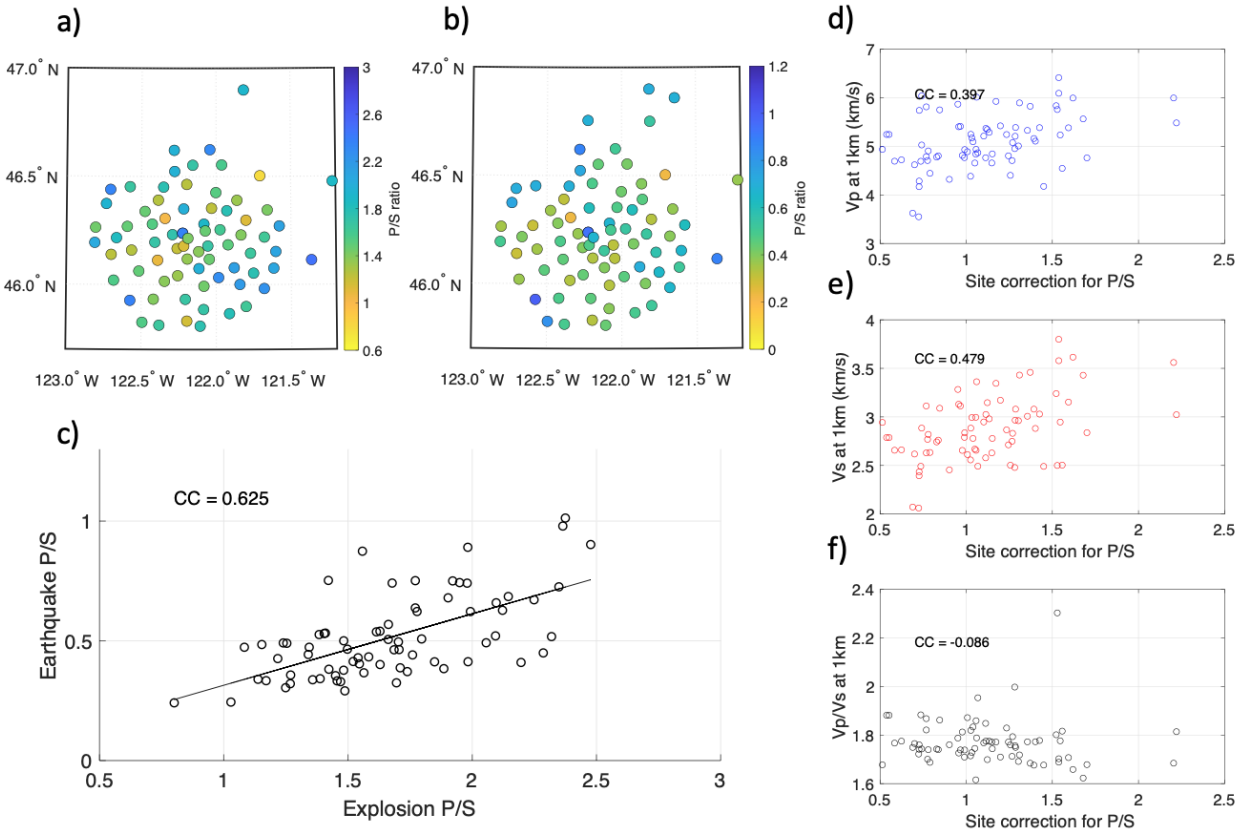


Figure 9. Site corrections and crustal seismic structure. A) Map of station-averaged P/S ratios for explosions. B) Map of station-averaged P/S ratios for earthquakes. Note that the color scale is different from A so that the similarity in spatial pattern is easier to identify. C) Scatter of station-averaged P/S ratios for earthquakes versus explosions. D-F) Scatter plots of site correction versus Vp, Vs, and Vp/Vs at 1 km depth from Ulberg et al., 2020. CC: cross-correlation coefficient.

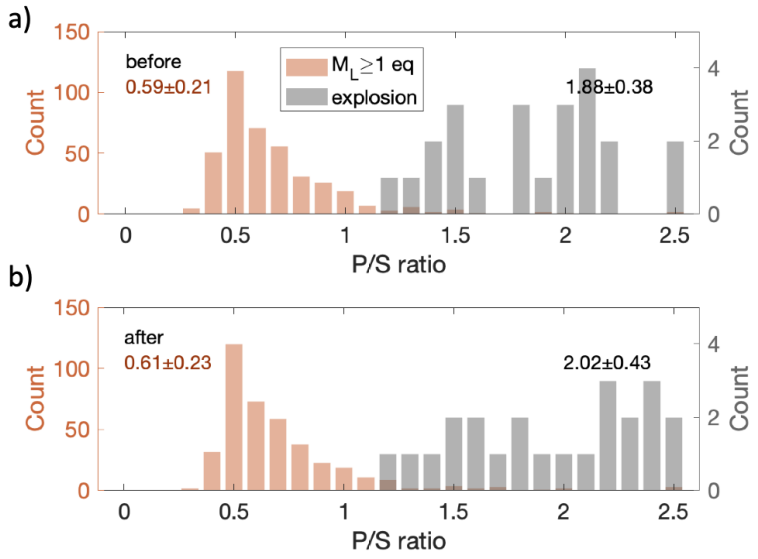


Figure 10. Site corrections and P/S ratios. A) Histograms of array-averaged P/S ratios for all explosions and earthquakes. B) Same as A, except the P/S site correction term is applied. The median±SMAD of the P/S ratio distributions are labeled in corresponding colors.

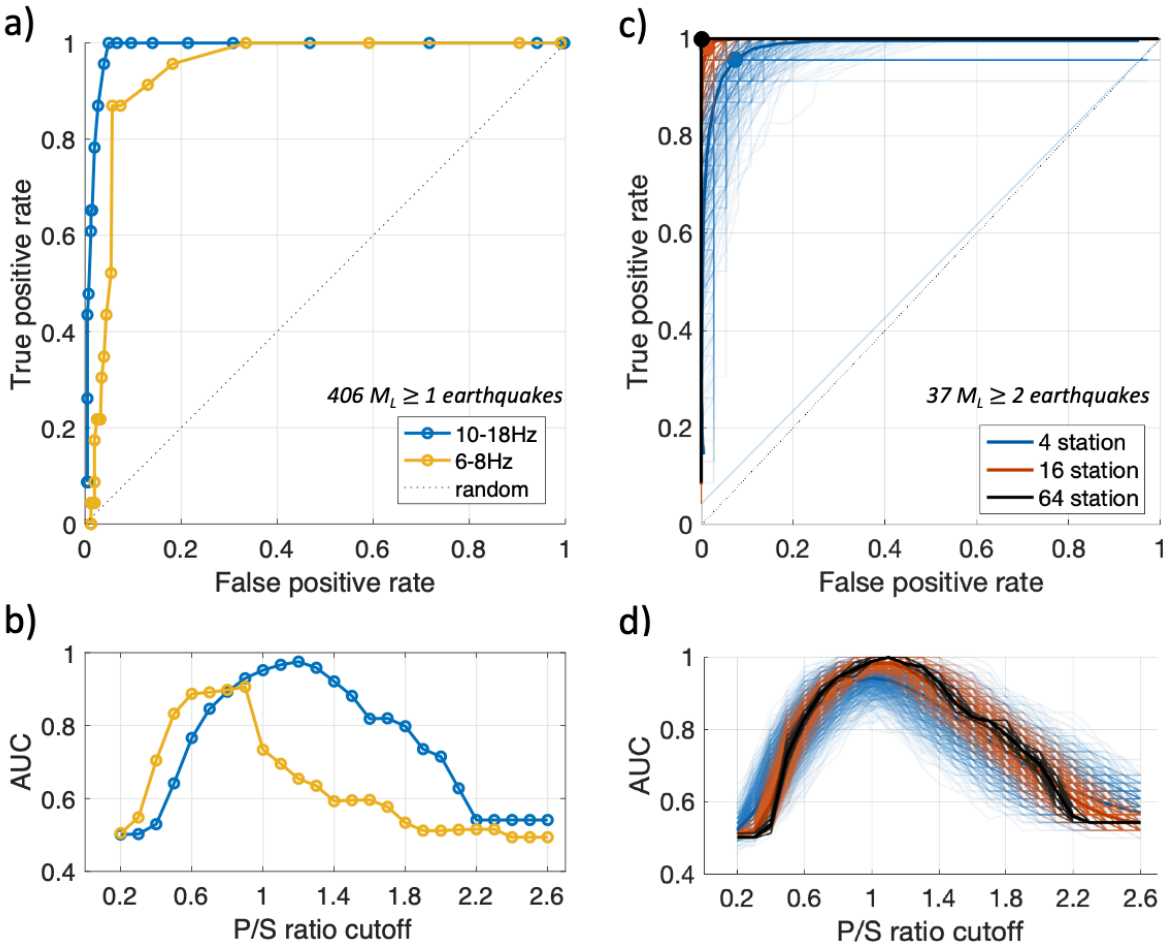


Figure 11. A) ROC curves for P/S ratio threshold optimization at 10-18 Hz and 6-8 Hz. B) Area under curve (AUC) for searched P/S ratio thresholds (0.1 step size from 0.2 to 2.6). The preferred P/S ratio cutoff is 1.2 at 10-18Hz (AUC=0.98), which leads to a true positive rate of 100% and false positive rate of 4.93%. C&D) Similar to A&B) but showing bootstrapping results using only $M_L \geq 2$ earthquakes. The bold lines are averaged curves from 1000 subsets and the three dots mark the highest AUC. Note that a few outliers exhibit near-random performance for the 4-station case (light blue near the diagonal in C) and a few others may reach AUC=1 while the averages (bold curves) are below 1 for 4-station and 16-station cases (in D).

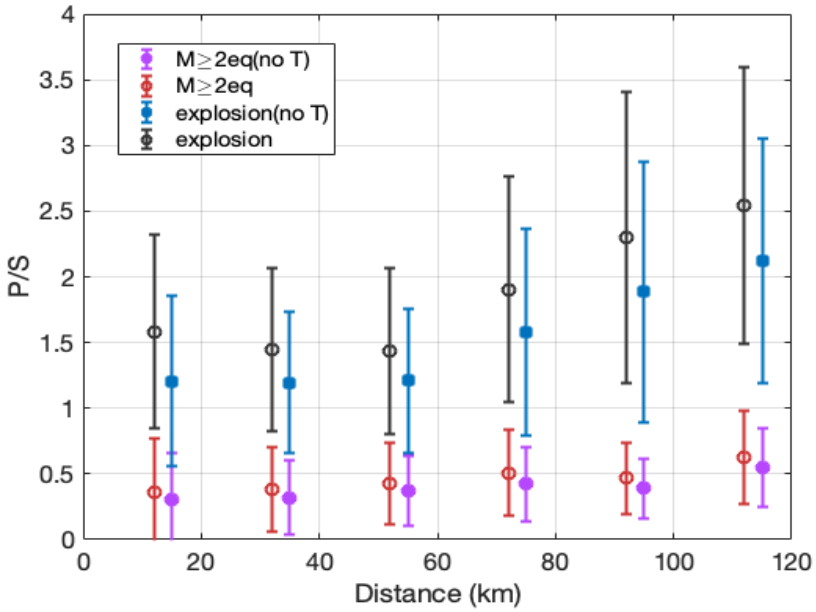


Figure 12. Effect of transverse component P-wave energy on P/S ratios. The error bars show medians and SMAD values of 10-18 Hz P/S ratios in 20 km bins for all source-station pairs (similar to Figure 6a but using only $M_L \geq 2$ earthquakes and all explosions).